Revision 1

Effects of hydrostaticity and Mn-substitution on dolomite stability at high pressure

Faxiang Wang[1], Chaoshuai Zhao[2,3]*, Liangxu Xu[2], Jin Liu[2,4]*

[1]Zhejiang Institute of Geological Survey, Hangzhou 311203, China

[2]Center for High Pressure Science and Technology Advanced Research, Beijing 100094, China

[3]Key Laboratory of Deep-Earth Dynamics of Ministry of Natural Resources, Institute of Geology, Chinese Academy of Geological Sciences, Beijing 100037, China

[4]CAS Center for Excellence in Deep Earth Science, Guangzhou 510640, China

*Correspondence to: C. Zhao (chaoshuai.zhao@hpstar.ac.cn) and J. Liu (jin.liu@hpstar.ac.cn)

Abstract

Studying the structural evolution of the dolomite group at high pressure is crucial for constraining the deep carbon cycle and mantle dynamics. Here we collected high-pressure laser Raman spectra of natural Mg-dolomite $CaMg(CO_3)_2$ and Mn-dolomite kutnohorite $Ca_{1.11}Mn_{0.89}(CO_3)_2$ samples up to 56 GPa at room temperature in a diamond anvil cell (DAC) using helium and neon as a pressure-transmitting medium (PTM), respectively. Using helium or neon can ensure samples stay under relatively hydrostatic conditions over the investigated pressure range, resembling the hydrostatic conditions of the deep mantle. Phase transitions in $CaMg(CO_3)_2$ were observed at 36.1(25) GPa in helium and 35.2(10) GPa in neon PTM for dolomite-II to -III, respectively. Moreover, the onset pressure of Mn-dolomite $Ca_{1.11}Mn_{0.89}(CO_3)_2$-III occurs at 23−25 GPa, about 10 GPa lower than that of Mg-dolomite-III, suggesting that cation substitution could significantly change the onset pressure of the phase

transitions in the dolomite group. These results provide new insights into deep carbon carriers within the Earth's mantle.

Keywords: Deep carbon cycle; Raman spectroscopy; high pressure; dolomite; phase transition

Introduction

Carbon geochemistry of mantle-derived material suggests that the flux of ca. 2.4−4.8 × 10^{13} g carbon enters the Earth's interior through subduction slabs each year (Dasgupta and Hirschmann, 2010; Plank and Manning, 2019). A part of carbon has been stored and transported into the deep mantle as accessory minerals (e.g., carbonates, diamond, and carbides) due to their relatively low solubility in silicates (Shcheka et al., 2006). Geochemical and petrologic evidence further indicates that carbon is mainly subducted as carbonate minerals under cold slab conditions, involving the crustal materials cycle and crust-mantle interaction (Sanchez-Valle et al., 2011). The presence of carbonate minerals can dramatically affect the physical and chemical properties of the mantle, such as phase stability, melting, viscosity, electrical conductivity, thermal conductivity, and elasticity (Fu et al., 2017; Gaillard et al., 2008; Yao et al., 2018; Zhao et al., 2019; Gui et al. 2021). Thus, studying the structural evolution of carbonate minerals at high pressure is crucial to constrain the deep carbon cycle as well as mantle dynamics (Farsang et al., 2021a; Fu et al., 2017; Isshiki et al., 2004; Liu et al., 2015; Mao et al., 2020; Sun et al., 2020; Zhao et al., 2021).

Among all the carbonate minerals subducting into the Earth's deep interior, the dolomite group (e.g., dolomite $CaMg(CO_3)_2$) has been extensively investigated as one of the most prominent deep carbon carriers. Some studies have proposed that dolomite could constitute up to 50% of the Earth's accessible carbonate reservoirs (Binck et al., 2020b). Moreover, given the chemical reactions with mantle minerals, $Ca(Mg,Fe,Mn)(CO_3)_2$ dolomite solid solutions with two or three metal cations are more realistic compositions for mantle carbonate minerals. The

partial cation substitution of Mg^{2+} by Fe^{2+} and Mn^{2+} is widely observed in natural dolomite samples (Efthimiopoulos et al., 2017; Richard and Wayne, 1989; Rividi et al., 2010). Furthermore, dolomite inclusions in super-deep diamonds evidence their existence in the deep mantle (Brenker et al., 2007; Logvinova et al., 2019).

Thus far, a good number of experiments and theoretical calculations have concentrated on the structure and phase transition of Mg,Fe-dolomite $Ca(Mg,Fe)(CO_3)_2$ under high pressures and/or high temperatures (Binck et al., 2020b; Efthimiopoulos et al., 2018; Mao et al., 2011; Merlini et al., 2012, 2017; Vennari and Williams, 2018; Zhao et al., 2020). A series of high-pressure phase transitions were reported from dolomite-I (abbreviated as Dol-I) to Dol-Ib at ~8−11 GPa, then to Dol-II at ~14−19 GPa, and subsequently to Dol-III at ~35−43 GPa with increasing pressure at room temperature (Binck et al., 2020b; Efthimiopoulos et al., 2017; Zhao et al., 2020). The Dol-IV and -V phases are only detected at simultaneous high temperature and pressure (*P*-*T*) conditions (Binck et al., 2020b; Merlini et al., 2017). In particular, those high-pressure phases of (Mg,Fe)-dolomite are considered to be important carbon carriers in the deep mantle (Mao et al., 2011; Merlini et al., 2012). Recently, it has been found that improved hydrostaticity can greatly influence the structural evolution of $MgCO_3$ at high pressure up to 80 GPa, where the pressure-transmitting medium (PTM) was helium (Zhao et al., 2021). However, the effects of hydrostaticity on those phase transitions in dolomite have not been investigated yet because of the lack of high-pressure studies on dolomite minerals using a helium PTM (Efthimiopoulos et al., 2018). Moreover, Raman spectra of Mn-dolomite kutnohorite $CaMn(CO_3)_2$ have not been reported at high pressure, and thus, the effects of the metal cation ratio (Ca^{2+}, Mg^{2+}, Fe^{2+}, Mn^{2+}) on the structure and phase transition in the dolomite minerals remain unclear under relatively hydrostatic conditions. Therefore, considering the hydrostatic conditions of the mantle, it is indispensable to know how the structure of the dolomite group evolves with increasing pressure under hydrostatic conditions.

In the present work, we carried out *in situ* Raman spectroscopic measurements on naturally

occurring Mg-dolomite $CaMg(CO_3)_2$ and Mn-dolomite $Ca_{1.11}Mn_{0.89}(CO_3)_2$ samples under high pressures up to 56 GPa in a diamond-anvil cell (DAC), with helium and neon as a PTM, respectively. Since the deep mantle is subjected to hydrostatic conditions, the use of helium allowed us to better understand the structural evolution of the dolomite group at high pressure. Compared to literature results under non-hydrostatic and quasi-hydrostatic conditions (Binck et al., 2020b; Efthimiopoulos et al., 2017, 2018; Merlini et al., 2017), a series of phase transitions in $CaMg(CO_3)_2$ and $Ca_{1.11}Mn_{0.89}(CO_3)_2$ were observed with increasing pressure. Furthermore, the onset pressure of these phase transitions in $Ca_{1.11}Mn_{0.89}(CO_3)_2$-III occurs at ~23−25 GPa, which is about 10 GPa lower than that of $CaMg(CO_3)_2$-III due to Mn-substitution. This result provides a better understanding of the structural behavior of carbonates at deep mantle conditions.

Experimental Methods

Starting materials

Natural single-crystal specimens of Mg- and Mn-dolomite samples were used as the starting materials. The Mg-dolomite sample was collected from Dabie Mountain, China, while the Mn-dolomite sample (Kutnohorite, no. NMNH148722) from the Sterling Hill (New Jersey, USA) was from the Department of Mineral Sciences, Smithsonian Institution. The chemical composition was determined using a JEOL JXA-8200 electron microprobe: $Ca_{1.0}Mg_{1.0}(CO_3)_2$ (with minor trace amounts of < 0.1 mol% Mn and Fe) for the Mg-dolomite sample and $Ca_{1.11}Mn_{0.89}(CO_3)_2$ for the Mn-dolomite sample. For simplicity, the Mg-dolomite sample is referred to as $CaMg(CO_3)_2$.

High-pressure Raman spectroscopy

High-pressure Raman spectra of $CaMg(CO_3)_2$ and $Ca_{1.11}Mn_{0.89}(CO_3)_2$ were collected between 100 and 1350 cm^{-1} using a Renishaw RM1000 Raman microscope at the Center for High Pressure Science and Technology Advanced Research (HPSTAR). The Raman spectrum

signal was excited using the 532 nm wavelength of an Ar^+ laser and collected through back-scattering geometry. The spectral resolution was ~2 cm^{-1} with a holographic diffraction grating of 1800 lines/mm. Please refer to our previous study for experimental information in detail (Zhao et al., 2021).

A symmetric DAC was mounted with two opposed diamond anvils with 300 μm flat culets. A sample chamber was drilled into the center of a pre-indented tungsten or rhenium gasket with a diameter of 180−200 μm and a thickness of ~30 μm. A platelet of single-crystal $CaMg(CO_3)_2$ with a thickness of 7–10 μm and ~50 μm in diameter was loaded into the sample chamber, together with a platelet of single-crystal $Ca_{1.11}Mn_{0.89}(CO_3)_2$ with a size comparable to Mg-dolomite. Two ruby spheres were then placed next to the samples for pressure calibration. The helium or neon PTM was loaded into the sample chamber using the high-pressure gas loading system at HPSTAR. The use of helium and neon maintains the quasi-hydrostatic conditions at 50 GPa, and thus, can avoid the influence of severe deviatoric stress in the sample chamber (Klotz et al., 2009). The pressure and uncertainties were calculated by multiple measurements of the ruby fluorescence before and after each Raman spectrum (Mao et al., 1986; Shen et al., 2020). Raman spectra were analyzed using the software PeakFit v4.12 with the Voigt area method.

Results and Discussion

Raman spectra of Mn-dolomite $Ca_{1.11}Mn_{0.89}(CO_3)_2$ and Mg-dolomite $CaMg(CO_3)_2$ were collected up to 56 GPa at room temperature in the helium PTM (Figures 1–4). Together with ankerite $Ca(Fe,Mg)(CO_3)_2$ and minrecordite $CaZn(CO_3)_2$, they belong to dolomite minerals. The dolomite group (space group $R\bar{3}$) is topologically identical to calcite, but in these double carbonate minerals, multiple different cations generally occupy alternate layers perpendicular to the *c* axis (Hazen et al., 2013). At ambient conditions, it has three lattice modes (one *T* and two *L* modes) and five internal modes (the in-plane bend internal (v_4), symmetric stretch internal (v_1),

anti-symmetric stretch (v_3), and out-of-plane bend (v_2 and $2v_2$) modes) (Farsang et al., 2018; Rividi et al., 2010). Therein, the two Raman-active modes v_3 and $2v_2$ are hardly observed at high pressure due to their relatively weak intensity through diamond anvils. The four strong, representative Raman peaks at 167, 287, 718, and 1088 cm^{-1} were observed for $Ca_{1.11}Mn_{0.89}(CO_3)_2$ at ambient conditions, corresponding to the *T*, *L*, v_4, and v_1 modes, respectively. These Raman modes are at 172, 291, 724, and 1094 cm^{-1} for $CaMg(CO_3)_2$. These values are systematically 4−10 cm^{-1} different from previously reported literature results (Farsang et al., 2018; Rividi et al., 2010). The difference largely comes from the varying chemical compositions of dolomite minerals. Besides, it should be noted that the *T* and *L* lattice modes result from the interactions between metal cation (Ca^{2+}, Mg^{2+}, Fe^{2+}, Mn^{2+}) and CO_3^{2-} ions, while the v_4 and v_1 modes are from the in-plane bending and symmetric stretching of the CO_3^{2-} units, respectively. These characteristics are identical to the calcite and dolomite groups, as previously reported (Farsang et al., 2018; Rividi et al., 2010).

Raman spectroscopy of $Ca_{1.11}Mn_{0.89}(CO_3)_2$ at high pressure

Representative high-pressure Raman spectra and Raman shifts of $Ca_{1.11}Mn_{0.89}(CO_3)_2$ are displayed in Figures 1−2 and Table 1. At ~13 GPa, several new *T* modes and *L* modes at 150−450 cm^{-1} appeared in $Ca_{1.11}Mn_{0.89}(CO_3)_2$, indicating a new structural modification. Based on the similarities in the Raman spectra between $Ca_{1.11}Mn_{0.89}(CO_3)_2$ and $CaMg(CO_3)_2$ (Binck et al., 2020b), it is denoted as the Dol-II phase in this study. Moreover, Palaich et al. (2015) reported a dramatic increase in the volume of Mn-rich dolomite sample $Ca_{0.76}Mn_{0.1.24}(CO_3)_2$ in a neon PTM at 15.9 GPa, associated with the disappearing and splitting of several diffraction lines in the powder x-ray diffraction (XRD) patterns. To some extent, this result supports the phase transition of Mn-dolomite revealed in the high-pressure evolution of Raman spectra in this study.

Upon further compression, the Dol-II phase enters another high-pressure phase of Mn-dolomite. Several Raman peaks, especially for the splitting of ν_1 mode, emerge at ~23−25

This is the peer-reviewed, final accepted version for American Mineralogist, published by the Mineralogical Society of America.
The published version is subject to change. Cite as Authors (Year) Title. American Mineralogist, in press.
DOI: https://doi.org/10.2138/am-2022-8248. http://www.minsocam.org/

GPa and remain to the highest pressure of this study (Figures 1−2). The new structure is referred to as the Dol-III phase following $Ca(Mg,Fe)(CO_3)_2$ (Binck et al., 2020b). In particular, the onset phase transition pressure of $Ca_{1.11}Mn_{0.89}(CO_3)_2$ from the Dol-II to -III is 23.4(13) GPa in helium and 25.3(8) GPa in neon, indicating a comparable effect of helium and neon PTMs on the evolution of $Ca_{1.11}Mn_{0.89}(CO_3)_2$ with increasing pressure. The onset Dol-III phase transition pressure of $Ca_{1.11}Mn_{0.89}(CO_3)_2$ is ~10 GPa lower than that of $CaMg(CO_3)_2$-III compressed in either helium or neon in this study (Table 2). It can be attributed to that Mn^{2+} (0.83 Å) has a much larger ionic radius than Mg^{2+} (0.72 Å) (Shannon, 1976). In other words, Mn-substitution could significantly alter the phase stability of dolomite minerals at high pressure. Moreover, such an effect is enhanced in single cation carbonate minerals. For instance, the onset pressure of $MnCO_3$-I to -II is at ~45 GPa, which is ~35 GPa lower than that of $MgCO_3$-I to -II under relatively hydrostatic conditions (Binck et al., 2020a; Liu et al., 2016; Zhao et al., 2021).

The Raman spectra and shifts of $Ca_{1.11}Mn_{0.89}(CO_3)_2$ change monotonically with increasing pressure in Dol-I, -II, and -III phases. Most of the Raman shifts increase with increasing pressure for each dolomite phase, whereas that of the the v_2 mode decrease upon compression (Figures 1−2 and Table 1). The pressure dependence values of Raman shift of each mode in Dol-III phase are much lower than these of Dol-I and -II phases, indicating a more rigid structure in Dol-III phase than these of Dol-I and -II.

Raman spectroscopy of $CaMg(CO_3)_2$ at high pressure

Representative high-pressure Raman spectra of $CaMg(CO_3)_2$ are shown in Figures 3−4. The phase boundary among Dol-I, -II and -III is not evidently presented in the Raman modes of $CaMg(CO_3)_2$ except ν_1 modes; therefore, here we only exhibited the change of ν_1 modes in Figure 4. Raman shifts of $CaMg(CO_3)_2$ increase monotonically with increasing pressure in Dol-I phase (Figure 3). Interestingly, the splitting of the *T* mode in $CaMg(CO_3)_2$ corresponding to the Dol-Ib phase was not observed in 0−16 GPa using helium as a PTM in this study. This result is in good

182 agreement with $CaMg_{0.92}Fe_{0.08}(CO_3)_2$ in the use of neon pressure medium (Vennari and Williams,
183 2018). On the contrary, in experiments using argon as a PTM, a clear splitting of the *T* mode was
184 observed at 8−11 GPa, which has been described as the Dol-Ib phase in different iron-bearing
185 dolomite compositions (Efthimiopoulos et al., 2017; Zhao et al., 2020). The contradictory
186 research results are due to a better hydrostatic environment in the sample chamber using helium
187 as the PTM in this study compared to argon in the previous studies. The latter exhibits
188 non-hydrostaticity at lower pressures and produces large deviatoric stress in the sample chamber
189 (Klotz et al., 2009). Moreover, the Dol-Ib phase was found in $CaMg_{0.92}Fe_{0.08}(CO_3)_2$ using a
190 mixture of KCl and neon as a PTM, while the Dol-Ib phase diminished after the sample was
191 annealed at ~1600 K in the same dolomite sample (Binck et al., 2020b). Those results suggest
192 good hydrostatic environments of helium or neon pressure medium would avoid the formation of
193 the Dol-Ib phase, enlarging the pressure range of the Dol-I phase. It evidently illustrates how
194 different PTMs influence the structure evolution of dolomite minerals.

195 Furthermore, the improved hydrostaticity from replacing a non-hydrostatic PTM (e.g., argon
196 and petroleum jelly) with helium exhibits a completely distinct effect on the phase stability of
197 Mg-dolomite $CaMg(CO_3)_2$ and magnesite $MgCO_3$. Magnesite undergoes magnesite-Ib and -Ic
198 (abbreviated as Mag-Ib and Mag-Ic) at ~30 and ~50 GPa in helium PTM, respectively (Zhao et
199 al., 2021), which are absent for magnesite in non-hydrostatic PTM (Binck et al., 2020a; Fiquet et
200 al., 2002; Williams et al., 1992). The difference in the structural evolution with pressure between
201 $CaMg(CO_3)_2$ and $MgCO_3$ may be attributed to the existence of alternate CaO_n layers in the
202 adjacent MgO_6 octahedra in $CaMg(CO_3)_2$ that could help adjust lattice distortion (Binck et al.,
203 2020b; Merlini et al., 2017).

204 New peaks and/or splitting of the ν_1 modes at ~1150−1250 cm^{-1} were both observed in
205 helium and neon PTMs at around 36 GPa (Figure 4). They are assigned as Dol-III in this study,
206 according to the previously reported Raman characteristics of dolomite (Binck et al., 2020b;
207 Efthimiopoulos et al., 2018; Vennari and Williams, 2018). Specifically, the single ν_1 mode

208 dramatically splits into the four modes at 1168, 1185, 1203, and 1228 cm^{-1} at ~36 GPa. It has
209 been ascribed to the formation of the Dol-III phase (Binck et al., 2020b; Efthimiopoulos et al.,
210 2018; Vennari and Williams, 2018; Zhao et al., 2020). Phase transitions in $CaMg(CO_3)_2$ were
211 observed at 36.1(25) GPa in helium and 35.2(10) GPa in neon PTM for dolomite-II to -III,
212 respectively. However, the onset phase transition pressure of $CaMg(CO_3)_2$ decreases by ~3 GPa
213 for the dolomite-III phases when argon and petroleum jelly were used as PTMs in previous
214 studies (Efthimiopoulos et al., 2017, 2018).

215 **The effect of cation radius on the structure of the dolomite group**

216 Together with the previously reported data on norsethite $BaMn(CO_3)_2$ and ankerite
217 $CaFe_{0.60}Mg_{0.40}(CO_3)_2$, the effects of the cation radius on the structure of dolomite minerals at
218 ambient conditions are revealed by our results of $CaMg(CO_3)_2$ and $Ca_{1.11}Mn_{0.89}(CO_3)_2$ (Figure 5).
219 In particular, $BaMn(CO_3)_2$, $CaMg(CO_3)_2$, and Fe-dolomite $CaFe_{0.60}Mg_{0.40}(CO_3)_2$ were chosen as
220 representative compositions. The cation radii of Ba^{2+}, Ca^{2+}, Mn^{2+}, Fe^{2+}, and Mg^{2+} are 1.35, 1.00,
221 0.83, 0.78, and 0.72 Å, respectively (Shannon, 1976). Raman shifts of the *T* and *L* modes for
222 $BaMn(CO_3)_2$ are much lower than that for $Ca_{1.11}Mn_{0.89}(CO_3)_2$ and $Ca(Fe,Mg)(CO_3)_2$ solid
223 solutions. The larger cation radius generally leads to the longer bonding length and weaker
224 chemical bond interactions between the metal cation and CO_3^{2-} group. It agrees well with the *T*
225 and *L* modes corresponding to lattice vibration. On the contrary, the differences in Raman peak
226 positions are less than 3 cm^{-1} among $CaMg(CO_3)_2$, $Ca_{1.02}(Mg_{0.78}Fe_{0.20})(CO_3)_2$, and
227 $Ca(Fe_{0.6}Mg_{0.4})(CO_3)_2$ at ambient conditions, suggesting that a small degree of Fe^{2+} substitution
228 for Mg^{2+} would not remarkably affect the structure of $Ca(Mg,Fe)(CO_3)_2$ solid solutions. Instead,
229 it is largely attributed to the identically occupied positions of Mg^{2+} and Fe^{2+} in the lattice and
230 similar cation radii (Lobanov and Goncharov, 2020; Shannon, 1976). Additionally, random
231 cation substitution would not lead to the loss of rotational symmetry for $Ca(Mg,Fe)(CO_3)_2$
232 (Merlini et al., 2017).

233 Furthermore, compared with the *T* and *L* modes, the v_1 mode seems to be the most insensitive

mode to the cation radius in the dolomite minerals group. The cation radii of Ba^{2+} and Mn^{2+} are much larger than that of Mg^{2+} and Fe^{2+}. However, the Raman shift of the v_1 mode in $BaMn(CO_3)_2$ is almost the same as that in $CaMg(CO_3)_2$. Such compositional effects are less evident in the internal modes (e.g., v_1), but more prominent in the external lattice modes (*T* and *L*). The difference among these modes may result from the covalent C-O bonds in the rhombohedral (CO_3^{2-}) group insensitive to cation substitution (Lin et al., 2012).

At ambient conditions, dolomite minerals display a strong and single v_1 stretching mode. In the Dol-III phase, the single v_1 mode splits into 3−4 Raman modes in $CaMg(CO_3)_2$ and $Ca_{1.11}Mn_{0.89}(CO_3)_2$ (Figure 6). The multiple v_1 modes in the Dol-III phase indicate a diversity of distorted structural environments and are assigned as the alternating distorted MgO_6 octahedra and distorted polyhedra of CaO_n ($7 \leqslant n \leqslant 9$) (Binck et al., 2020b). Here, we compare representative Raman spectra of $CaMg(CO_3)_2$ and $Ca_{1.11}Mn_{0.89}(CO_3)_2$ at 50.0 GPa and 300 K using helium as a PTM due to the lack of high-pressure Raman data on $BaMn(CO_3)_2$ and Fe-dolomite. Compared with the v_1 mode of $CaMg(CO_3)_2$ and $Ca_{1.11}Mn_{0.89}(CO_3)_2$ in the Dol-III, there may be two different kinds of CO_3^{2-} group environment. $CaMg(CO_3)_2$ exhibits four v_1 bands while there are three v_1 bands for $Ca_{1.11}Mn_{0.89}(CO_3)_2$. This result indicates that the atomic structure of CO_3^{2-} groups in $Ca_{1.11}Mn_{0.89}(CO_3)_2$ may be slightly different from that in $CaMg(CO_3)_2$. A high-pressure XRD study on $Ca_{1.11}Mn_{0.89}(CO_3)_2$ will be conducted in the near future to clarify this difference.

The effect of cation ratio on the phase transitions of $Ca(Mg,Fe,Mn)(CO_3)_2$

Four groups of different cation compositions are compiled in Figure 7 to study the effect of different cation ratios on the phase transitions of $Ca(Mg,Fe,Mn)(CO_3)_2$ solid solutions. The experimental results using helium or neon were selected to exclude the effect of non-hydrostaticity (Table 2). We note that the onset phase transition pressure between the Dol-I and Dol-II was determined by the highest pressure point of the Dol-I and the lowest pressure

point of the Dol-II. The onset pressures of the Dol-II and Dol-III were separately fitted with each cation ratio at room temperature (Figure 7). In general, the onset phase transition pressure of dolomite from the Dol-I to the Dol-II phase seems insensitive to the type of metal cations (e.g., Mg^{2+}, Fe^{2+}, and Mn^{2+}), except for Ca^{2+}. On the contrary, the onset pressure of the Dol-II to Dol-III phase is more sensitive to Mg^{2+}, Mn^{2+}, and Ca^{2+}, but not to Fe^{2+}. The slopes of the onset phase transition pressure of the Dol-II to Dol-III with increasing cation concentration of Mg^{2+}, Mn^{2+}, and Ca^{2+} are 0.28(5), −0.30(4), and −2.31(33) GPa per mol%, respectively (Figure 7).

Implications

The phase transition of single divalent metal carbonates (e.g., $CaCO_3$, $MgCO_3$, $FeCO_3$, and $MnCO_3$) is greatly affected by compositional variation (Liu et al., 2016). Such an effect is much weaker in multiple metal cation carbonates including $CaMg(CO_3)_2$, $Ca(Mg,Fe)(CO_3)_2$, $CaMn(CO_3)_2$, and $Na_2Ca_2(CO_3)_3$. Notably, the onset pressure of the phase transition from the Dol-II to -III in $Ca_{1.11}Mn_{0.89}(CO_3)_2$ is ~10 GPa lower than that in $CaMg(CO_3)_2$. This result reveals the important effect of cation radius on the kinetics of pressure-induced structure transformations. The substitution by a larger metal cation in carbonate minerals could lower the kinetic barriers of phase transitions, and thus, carbonate minerals with larger metal cations enter high-pressure phases at relatively lower pressures.

Furthermore, the single v_1 mode splitting into multiple modes in $CaMg(CO_3)_2$ and $Ca_{1.11}Mn_{0.89}(CO_3)_2$ in the Dol-III structure is particularly interesting. The multiple v_1 modes in the Dol-III phase indicate a diversity of distorted structural environments and are ascribed to the alternately distorted MgO_6 octahedra and distorted polyhedra of CaO_n ($7 \leqslant n \leqslant 9$) (Binck et al., 2020b). Single metal cation carbonates such as $MgCO_3$ and $MnCO_3$ undergo an analogous distorted structure at higher pressures of above 80 GPa (Binck et al., 2020a; Boulard et al., 2011; Cerantola et al., 2017; Oganov et al., 2008), whereas distorted structures of multiple metal cation carbonates such as $CaSrCO_3$ and $Na_2Ca_2(CO_3)_3$ occur at low pressures of ~4−15 GPa

(Martirosyan et al., 2021; Vennari et al., 2018). The distorted structural environments provide a potential way to transport carbon into the deep mantle through a plethora of high-pressure polymorphisms of carbonate minerals due to diverse bonding patterns for carbon (Boulard et al., 2020; Lobanov and Goncharov, 2020). Meanwhile, these crystallographic characteristics of carbonates likely play an important role in the storage or transportation of incompatible elements (e.g., K, Ba, Sr) and trace elements (e.g., Zn, Co, Ni, Cd) in the deep mantle, as evidenced by syngenetic diamond inclusions and high temperature and high pressure experiment simulation (Farsang et al., 2021b, 2021c; Frezzotti et al., 2011; Logvinova et al., 2008, 2011).

The PTMs in high-pressure experiments play a key role in the structural evolution and phase stability of carbonate minerals. Interestingly, the effects of PTMs are different among varying metal cation carbonates (Efthimiopoulos et al., 2018; Liu et al., 2016; Zhao et al., 2018). In the present work, high-pressure vibrational properties of two natural single-crystal samples of $CaMg(CO_3)_2$ and $Ca_{1.11}Mn_{0.89}(CO_3)_2$ were investigated up to 56 GPa at room temperature in DACs using helium and neon as PTMs. The Dol-Ib phase was not observed due to the improved hydrostaticity in the sample chamber, extending the stable pressure range of the Dol-I phase of the dolomite group at room temperature for dolomite (Binck et al., 2020b; Efthimiopoulos et al., 2017). On the contrary, the Mag-Ib and Mag-Ic phases are only observed in the helium PTM (Zhao et al., 2021) but not in non-hydrostatic PTMs (e.g., argon and methanol-ethanol 4:1 mixture) (Fiquet et al., 2002; Williams et al., 1992). Moreover, non-hydrostaticity generally reduces the onset phase transition pressure due to large deviatoric stress. Compared with the phase stability of $MnCO_3$ between helium/neon and NaCl/silicone oil PTMs, the onset phase transition pressures of $MnCO_3$ are increased by ~30 and ~13 GPa for the $MnCO_3$-I + II mixture and the $MnCO_3$-II phase, respectively (Boulard et al., 2015; Liu et al., 2016; Merlini et al., 2015; Zhao et al., 2018). Remarkably, compared to previous studies on $CaMg_{0.98}Fe_{0.02}(CO_3)_2$ compressed in a petrleum jellly or argon PTM (Efthimiopoulos et al., 2017, 2018), the improved hydrostaticity with the use of helium and neon in this study exhibites a similar onset phase

transition pressure of dolo-III $CaMg(CO_3)_2$ (Binck et al., 2020b; Merlini et al., 2017). Therefore, the stress environment of different PTMs in the sample chamber displays complex influences on the phase stability of carbonate minerals. Given the relatively hydrostatic conditions of the Earth's mantle, hydrostaticity shall be considered for better understanding the deep carbon cycle.

Acknowledgments

This study is funded by the National Key Research and Development Program of China (2019YFA0708502). C. Zhao acknowledges support from the National Natural Science Foundation of China (NSFC grant no. 42104101) and open fund from the Key Laboratory of Deep-Earth Dynamics of the Ministry of Natural Resource, Institute of Geology, Chinese Academy of Geological Sciences (J1901-16). Some experiments are supported by the Synergic Extreme Condition User Facility (SECUF). The Department of Mineral Sciences, Smithsonian Institution is acknowledged for the Mn-dolomite sample (Kutnohorite, no. NMNH148722).

References

Binck, J., Bayarjargal, L., Lobanov, S.S., Morgenroth, W., Luchitskaia, R., Pickard, C.J., Milman, V., Refson, K., Jochym, D.B., Byrne, P., and Winkler, B. (2020a) Phase stabilities of $MgCO_3$ and $MgCO_3$-II studied by Raman spectroscopy, x-ray diffraction, and density functional theory calculations. Physical Review Materials, 4(5), 0055001-1−0055001-9.

Binck, J., Chariton, S., Stekiel, M., Bayarjargal, L., Morgenroth, W., Milman, V., Dubrovinsky, L., and Winkler, B. (2020b) High-pressure, high-temperature phase stability of iron-poor dolomite and the structures of dolomite-IIIc and dolomite-V. Physics of the Earth and Planetary Interiors, 299, 106403.

Boulard, E., Gloter, A., Corgne, A., Antonangeli, D., Auzende, A.L., Perrillat, J.P., Guyot, F., and Fiquet, G. (2011) New host for carbon in the deep Earth. Proceeding of the National Academy of Sciences of the United States of America, 108(13), 5184-5187.

Boulard, E., Goncharov, A.F., Blanchard, M., and Mao, W.L. (2015) Pressure-induced phase transition in $MnCO_3$ and its implications on the deep carbon cycle. Journal of Geophysical Research: Solid Earth, 120(6), 4069-4079.

Boulard, E., Guyot, F., and Fiquet, G. (2020) High-pressure transformations and stability of ferromagnesite in the Earth's mantle. Carbon in Earth's Interior, 105-113.

Brenker, F.E., Vollmer, C., Vincze, L., Vekemans, B., Szymanski, A., Janssens, K., Szaloki, I., Nasdala, L., Joswig, W., Kaminsky, F. (2007) Carbonates from the lower part of transition zone or even the lower mantle. Earth and Planetary Science Letters, 260(1-2), 1-9.

Cerantola, V., Bykova, E., Kupenko, I., Merlini, M., Ismailova, L., McCammon, C., Bykov, M., Chumakov, A.I., Petitgirard, S., Kantor, I., Svitlyk, V., Jacobs, J., Hanfland, M., Mezouar, M., Prescher, C., Ruffer, R., Prakapenka, V.B., and Dubrovinsky, L. (2017) Stability of iron-bearing carbonates in the deep Earth's interior. Nature Communications, 8, 15960.

Dasgupta, R., and Hirschmann, M.M. (2010) The deep carbon cycle and melting in Earth's interior. Earth and Planetary Science Letters, 298(1-2), 1-13.

Efthimiopoulos, I., Germer, M., Jahn, S., Harms, M., Reichmann, H.J., Speziale, S., Schade, U., Sieber, M., and Koch-Müller, M. (2018) Effects of hydrostaticity on the structural stability of carbonates at lower mantle pressures: the case study of dolomite. High Pressure Research, 1-14.

Efthimiopoulos, I., Jahn, S., Kuras, A., Schade, U., and Koch-Müller, M. (2017) Combined high-pressure and high-temperature vibrational studies of dolomite: phase diagram and evidence of a new distorted modification. Physics and Chemistry of Minerals, 44(7), 465-476.

Farsang, S., Facq, S., and Redfern, S. (2018) Raman modes of carbonate minerals as pressure and temperature gauges up to 6 GPa and 500 °C. American Mineralogist, 103, 1988–1998.

Farsang, S., Louvel, M., Zhao, C., Mezouar, M., Rosa, A.D., Widmer, R.N., Feng, X., Liu, J., and Redfern, S.A.T. (2021a) Deep carbon cycle constrained by carbonate solubility. Nature Communications, 12(1), 4311.

Farsang, S., Louvel, M., Rosa, A.D., Amboage, M., Anzellini, S., Widmer, R.N., and Redfern, S.A.T. (2021b) Effect of salinity, pressure and temperature on the solubility of smithsonite ($ZnCO_3$) and Zn complexation in crustal and upper mantle hydrothermal fluids. Chemical Geology, 578, 120320.

Farsang, S., Widmer, R.N., and Redfern, S.A.T. (2021c) High-pressure and high-temperature vibrational properties and anharmonicity of carbonate minerals up to 6 GPa and 500 °C by Raman spectroscopy. American Mineralogist, 106(4), 581-598.

Fiquet, G., Guyot, F., Kunz, M., Matas, J., Andrault, D., and Hanfland, M. (2002) Structural refinements of magnesite at very high pressure. American Mineralogist, 87(8-9), 1261-1265.

Fu, S., Yang, J., and Lin, J.F. (2017) Abnormal elasticity of single-crystal magnesiosiderite across the spin transition in Earth's lower mantle. Physical Review Letters, 118(3), 036402.

Gaillard, F., Malki, M., Iacono-Marziano, G., Pichavant, M., and Scaillet, B. (2008) Carbonatite melts and electrical conductivity in the asthenosphere. Science, 322(5906), 1363-1365.

Gui, W.B, Zhao, C.S., Liu, J., Phase stability and hydroxyl vibration of brucite $Mg(OH)_2$ at high pressure and high temperature. Chinese Physics Letters, 2021, 38: 038101.

Hazen, R.M., Downs, R.T., Jones, A.P., and Kah, L. (2013) Carbon mineralogy and crystal chemistry. Reviews in Mineralogy and Geochemistry, 75(1), 7-46.

Isshiki, M., Irifune, T., Hirose, K., Ono, S., Ohishi, Y., Watanuki, T., Nishibori, E., Takata, M., and Sakata, M. (2004) Stability of magnesite and its high-pressure form in the lowermost mantle. Nature, 427(6969), 60-63.

Klotz, S., Chervin, J.C., Munsch, P., and Le Marchand, G. (2009) Hydrostatic limits of 11 pressure transmitting media. Journal of Physics D: Applied Physics, 42(7), 075413.

Liang, W., Li, L., Yin, Y., Li, R., Li, Z., Liu, X., Zhao, C., Yang, S., Meng, Y., Li, Z., He, Y., and Li, H. (2019) Crystal structure of norsethite-type $BaMn(CO_3)_2$ and its pressure-induced transition investigated by Raman spectroscopy. Physics and Chemistry of Minerals, 46(8), 771-781.

Lin, J.F., Liu, J., Jacobs, C., and Prakapenka, V.B. (2012) Vibrational and elastic properties of ferromagnesite across the electronic spin-pairing transition of iron. American Mineralogist, 97(4), 583-591.

Liu, J., Caracas, R., Fan, D., Bobocioiu, E., Zhang, D., and Mao, W.L. (2016) High-pressure compressibility and vibrational properties of $(Ca,Mn)CO_3$. American Mineralogist, 101(12), 2723-2730.

Liu, J., Lin, J.F., and Prakapenka, V.B. (2015) High-pressure orthorhombic ferromagnesite as a potential deep-mantle carbon carrier. Scientific Reports, 5, 7640.

Lobanov, S.S., Goncharov, A. F. (2020) Pressure-induced sp^2-sp^3 transitions in carbon-bearing phases. Carbon in Earth's Interior, 1-9.

Logvinova, A.M., Shatskiy, A., Wirth, R., Tomilenko, A.A., Ugap'eva, S.S., and Sobolev, N.V. (2019) Carbonatite melt in type Ia gem diamond. Lithos, 342-343, 463-467.

Logvinova, A.M., Wirth, R., Fedorova, E.N., and Sobolev, N.V. (2008) Nanometre-sized mineral and fluid inclusions in cloudy Siberian diamonds: new insights on diamond formation. European Journal of Mineralogy, 20(3), 317-331.

Logvinova, A.M., Wirth, R., Tomilenko, A.A., Afanas'ev, V.P., and Sobolev, N.V. (2011) The phase composition of crystal-fluid nanoinclusions in alluvial diamonds in the northeastern Siberian Platform. Russian Geology and Geophysics, 52(11), 1286-1297.

Mao, H.K., Xu, J., and Bell, P.M. (1986) Calibration of the ruby pressure gauge to 800 kbar under quasi-hydrostatic conditions. Journal of Geophysical Research, 91(B5), 4673.

Mao, H.-K., and Mao, W.L. (2020) Key problems of the four-dimensional Earth system. Matter and Radiation at Extremes, 5(3), 038102.

Mao, Z., Armentrout, M., Rainey, E., Manning, C.E., Dera, P., Prakapenka, V.B., and Kavner, A. (2011) Dolomite III: A new candidate lower mantle carbonate. Geophysical Research Letters, 38(22), L22303.

Martirosyan, N.S., Efthimiopoulos, I., Pennacchioni, L., Wirth, R., Jahn, S., and Koch-Müller, M. (2021) Effect of cationic substitution on the pressure-induced phase transitions in calcium carbonate. American Mineralogist, 106(4), 549-558.

Merlini, M., Cerantola, V., Gatta, G.D., Gemmi, M., Hanfland, M., Kupenko, I., Lotti, P., Müller, H., and Zhang, L. (2017) Dolomite-IV: Candidate structure for a carbonate in the Earth's lower mantle. American Mineralogist, 102(8), 1763-1766.

Merlini, M., Crichton, W.A., Hanfland, M., Gemmi, M., Muller, H., Kupenko, I., and Dubrovinsky, L. (2012) Structures of dolomite at ultrahigh pressure and their influence on the deep carbon cycle. Proceedings of the National Academy of Sciences of the United States of America, 109(34), 13509-14.

Merlini, M., Hanfland, M., and Gemmi, M. (2015) The $MnCO_3$-II high-pressure polymorph of rhodocrosite. American Mineralogist, 100(11-12), 2625-2629.

Oganov, A.R., Ono, S., Ma, Y., Glass, C.W., and Garcia, A. (2008) Novel high-pressure structures of $MgCO_3$, $CaCO_3$ and CO_2 and their role in Earth's lower mantle. Earth and Planetary Science Letters, 273(1-2), 38-47.

Palaich, S.E.M., Heffern, R.A., Watenphul, A., Knight, J., and Kavner, A. (2015) High-pressure compressibility and phase stability of Mn-dolomite (kutnohorite). American Mineralogist, 100(10), 2242-2245.

Plank, T., and Manning, C.E. (2019) Subducting carbon. Nature, 574(7778), 343-352.

Richard J.R., Wayne, A.D. (1989) Structural variation in the dolomite-ankerite solid-solution series An X-ray, Miissbauer, and TEM study. American Mineralogist, 74(9-10), 1159–1167.

Rividi, N., van Zuilen, M., Philippot, P., Menez, B., Godard, G., and Poidatz, E. (2010) Calibration of carbonate composition using micro-Raman analysis: application to planetary surface exploration. Astrobiology, 10(3), 293-309.

Sanchez-Valle, C., Ghosh, S., and Rosa, A.D. (2011) Sound velocities of ferromagnesian carbonates and the seismic detection of carbonates in eclogites and the mantle. Geophysical Research Letters, 38(24), L24315.

Shannon, R.D. (1976) Revised effective ionic radii and systematic studies of interatomic distances in halides and chalcogenides. Acta Crystallographica, A32, 751-767.

Shcheka, S.S., Wiedenbeck, M., Frost, D.J., and Keppler, H. (2006) Carbon solubility in mantle minerals. Earth and Planetary Science Letters, 245(3-4), 730-742.

Shen, G., Wang, Y., Dewaele, A., Wu, C., Fratanduono, D.E., Eggert, J., Klotz, S., Dziubek, K.F., Loubeyre, P., Fat'yanov, O.V., Asimow, P.D., Mashimo, T., and Wentzcovitch, R.M.M. (2020) Toward an international practical pressure scale: A proposal for an IPPS ruby gauge (IPPS-Ruby2020). High Pressure Research, 40(3), 299-314.

Sun, Y., Hier-Majumder, S., Xu, Y., and Walter, M. (2020) Stability and migration of slab-derived carbonate-rich melts above the transition zone. Earth and Planetary Science Letters, 531, 116000.

Vennari, C.E., Beavers, C.M., and Williams, Q. (2018) High-pressure/temperature behavior of the alkali/calcium carbonate shortite ($Na_2Ca_2(CO_3)_3$): Implications for carbon sequestration in Earth's transition zone. Journal of Geophysical Research: Solid Earth, 123(8), 6574-6591.

Vennari, C.E., and Williams, Q. (2018) A novel carbon bonding environment in deep mantle high-pressure dolomite. American Mineralogist, 103(1), 171-174.

Williams, Q., Collerson, B., and Knittle, E. (1992) Vibrational spectra of magnesite ($MgCO_3$) and calcite-III at high pressures. American Mineralogist, 77(11-12), 1158-1165.

Yao, C., Wu, Z., Zou, F., and Sun, W. (2018) Thermodynamic and elastic properties of magnesite at mantle conditions: First-principles calculations. Geochemistry, Geophysics, Geosystems, 19(8), 2719-2731.

Zhao, C., Li, H., Chen, P., and Jiang, J. (2019) Sound velocities across calcite phase transitions by Brillouin scattering spectroscopy. American Mineralogist, 104(3), 418-424.

Zhao, C., Li, H., Jiang, J., He, Y., and Liang, W. (2018) Phase Transition and vibration properties of $MnCO_3$ at high pressure and high-temperature by Raman spectroscopy. High Pressure Research, 38(3), 212-223.

Zhao, C., Lv, C., Xu, L., Liang, L., and Liu, J. (2021) Raman signatures of the distortion and stability of $MgCO_3$ to 75 GPa. American Mineralogist, 106(3), 367-373.

Zhao, C., Xu, L., Gui, W., and Liu, J. (2020) Phase stability and vibrational properties of iron-bearing carbonates at high pressure. Minerals, 10(12), 1142.

Zucchini, A., Comodi, P., Nazzareni, S., and Hanfland, M. (2014) The effect of cation ordering and temperature on the high-pressure behaviour of dolomite. Physics and Chemistry of

Minerals, 41(10), 783-793.

This is the peer-reviewed, final accepted version for American Mineralogist, published by the Mineralogical Society of America.
The published version is subject to change. Cite as Authors (Year) Title. American Mineralogist, in press.
DOI: https://doi.org/10.2138/am-2022-8248. http://www.minsocam.org/

485 **Figure Captions**

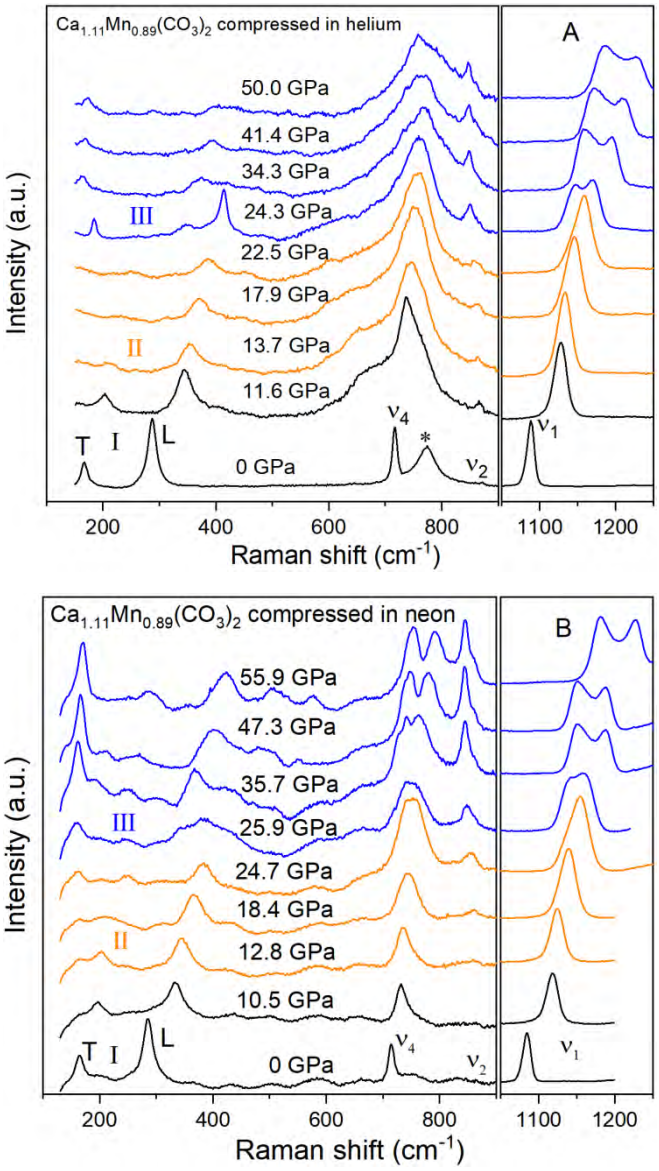

486

487

488 **Figure 1.** Representative Raman spectra of $Ca_{1.11}Mn_{0.89}(CO_3)_2$ as a function of pressure at room
489 temperature in helium (A) and neon (B) pressure transmitting media. The peak marked with an
490 asterisk symbol (*) represents the background signal of the Raman spectroscopic system. Black,
491 orange, and blue represent Dol-I, -II, -III phases of $Ca_{1.11}Mn_{0.89}(CO_3)_2$, respectively.

492

This is the peer-reviewed, final accepted version for American Mineralogist, published by the Mineralogical Society of America.
The published version is subject to change. Cite as Authors (Year) Title. American Mineralogist, in press.
DOI: https://doi.org/10.2138/am-2022-8248. http://www.minsocam.org/

493

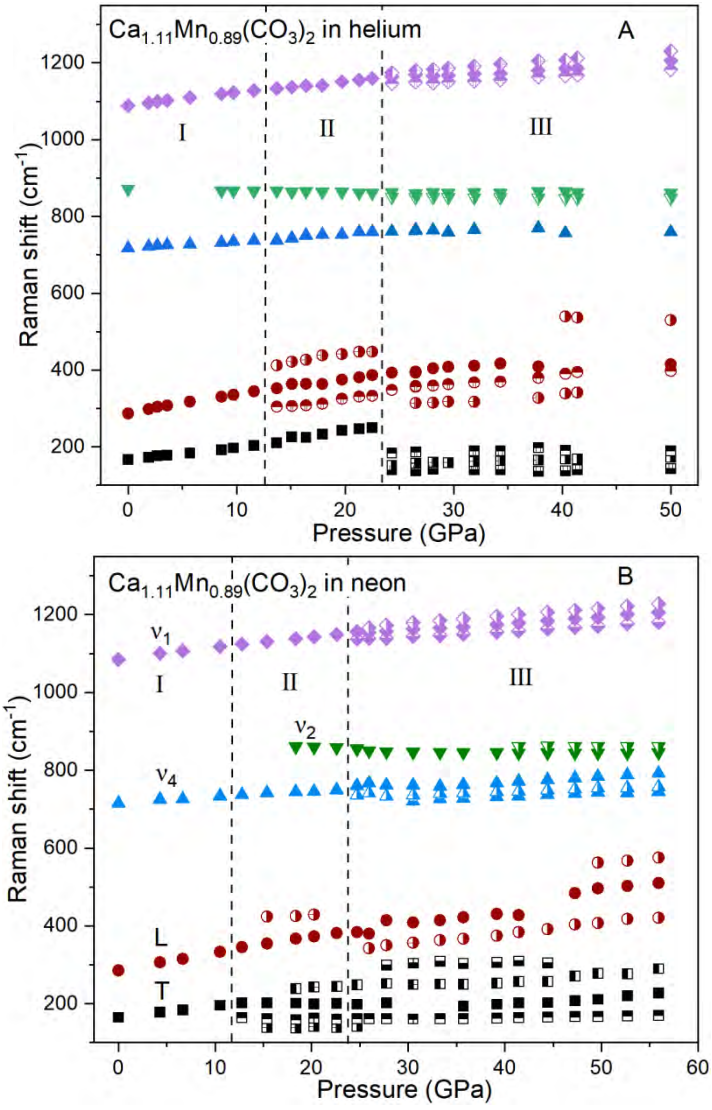

494

495

496 **Figure 2.** Raman shifts of $Ca_{1.11}Mn_{0.89}(CO_3)_2$ as a fucntion of pressure at room temperature. The
497 balck dashed lines denote the phase boundary among I, II and III in $Ca_{1.11}Mn_{0.89}(CO_3)_2$.

498

This is the peer-reviewed, final accepted version for American Mineralogist, published by the Mineralogical Society of America.
The published version is subject to change. Cite as Authors (Year) Title. American Mineralogist, in press.
DOI: https://doi.org/10.2138/am-2022-8248. http://www.minsocam.org/

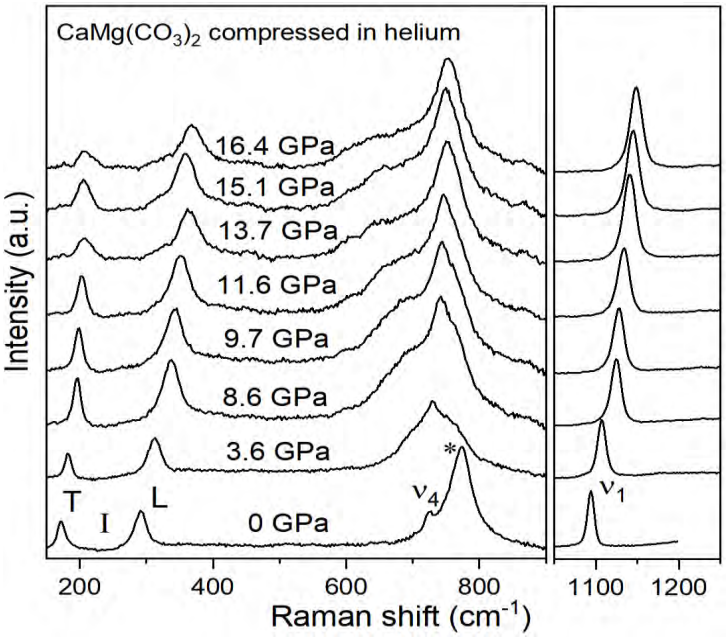

Figure 3. Representative Raman spectra of $CaMg(CO_3)_2$ as a function of pressure at room temperature in helium pressure-transmitting medium. The peak marked with an asterisk symbol (*) represents the background signal of the Raman spectroscopic system.

This is the peer-reviewed, final accepted version for American Mineralogist, published by the Mineralogical Society of America.
The published version is subject to change. Cite as Authors (Year) Title. American Mineralogist, in press.
DOI: https://doi.org/10.2138/am-2022-8248. http://www.minsocam.org/

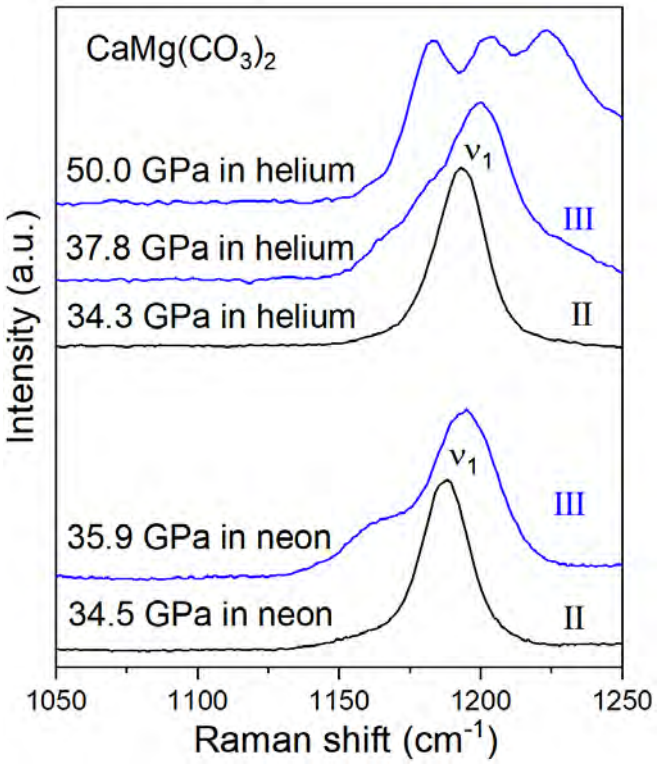

505

506

507 **Figure 4.** Representative Raman spectra of $CaMg(CO_3)_2$ as a function of pressure in helium and

508 neon at room temperature.

509

This is the peer-reviewed, final accepted version for American Mineralogist, published by the Mineralogical Society of America.
The published version is subject to change. Cite as Authors (Year) Title. American Mineralogist, in press.
DOI: https://doi.org/10.2138/am-2022-8248. http://www.minsocam.org/

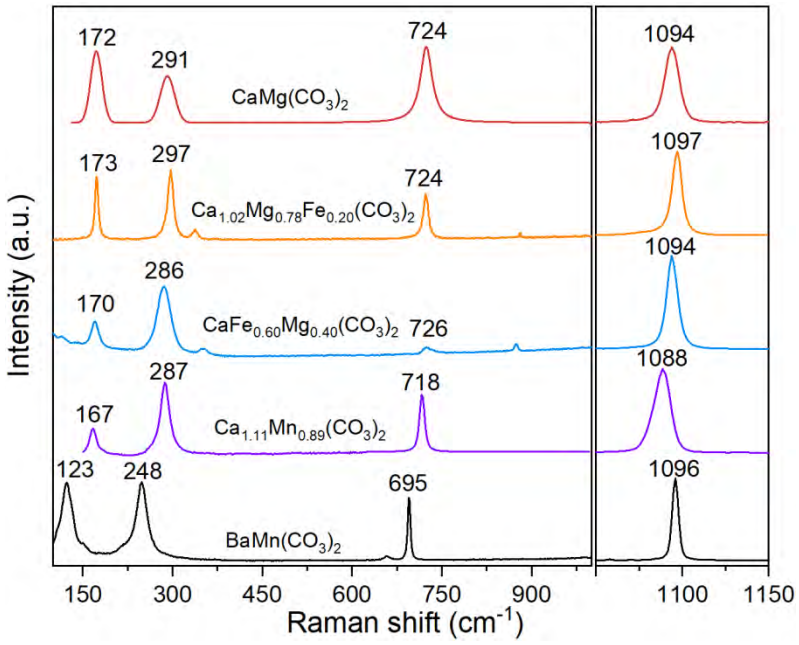

Figure 5. The effect of double cation radius on the Raman shifts of dolomite minerals at ambient conditions. Cation radius: $R(Ba^{2+})$ = 1.35 Å, $R(Ca^{2+})$ = 1.00 Å, $R(Mn^{2+})$ = 0.83 Å, $R(Fe^{2+})$ = 0.78 Å, $R(Mg^{2+})$ = 0.72 Å. Red and purple curves: $CaMg(CO_3)_2$ and $Ca_{1.11}Mn_{0.89}(CO_3)_2$, respectively, this study; orange curve: $Ca_{1.02}Mg_{0.78}Fe_{0.20}(CO_3)_2$, Zhao et al. (2020); black curve: $BaMn(CO_3)_2$, Liang et al. (2019); blue curve: $CaFe_{0.60}Mg_{0.40}(CO_3)_2$, RRUFF database (RRUFF ID: R050181.2).

This is the peer-reviewed, final accepted version for American Mineralogist, published by the Mineralogical Society of America.
The published version is subject to change. Cite as Authors (Year) Title. American Mineralogist, in press.
DOI: https://doi.org/10.2138/am-2022-8248. http://www.minsocam.org/

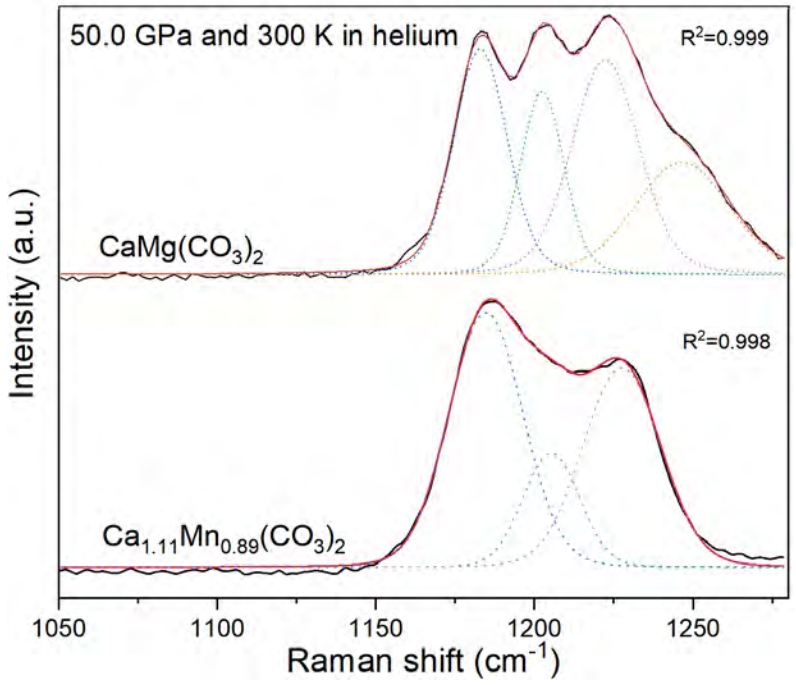

519

520

521 **Figure 6.** Representative Raman spectra of $CaMg(CO_3)_2$-III and $Ca_{1.11}Mn_{0.89}(CO_3)_2$-III phases at
522 50.0 GPa and room temperature. Helium was used as the pressure-transmitting medium. Black
523 and red curves: experimental data and fitting of Raman spectra, respectively, for $CaMg(CO_3)_2$-III
524 and $Ca_{1.11}Mn_{0.89}(CO_3)_2$-III; dotted curves: Raman peaks fitting using peakFit v4.12.

525

This is the peer-reviewed, final accepted version for American Mineralogist, published by the Mineralogical Society of America.
The published version is subject to change. Cite as Authors (Year) Title. American Mineralogist, in press.
DOI: https://doi.org/10.2138/am-2022-8248. http://www.minsocam.org/

526

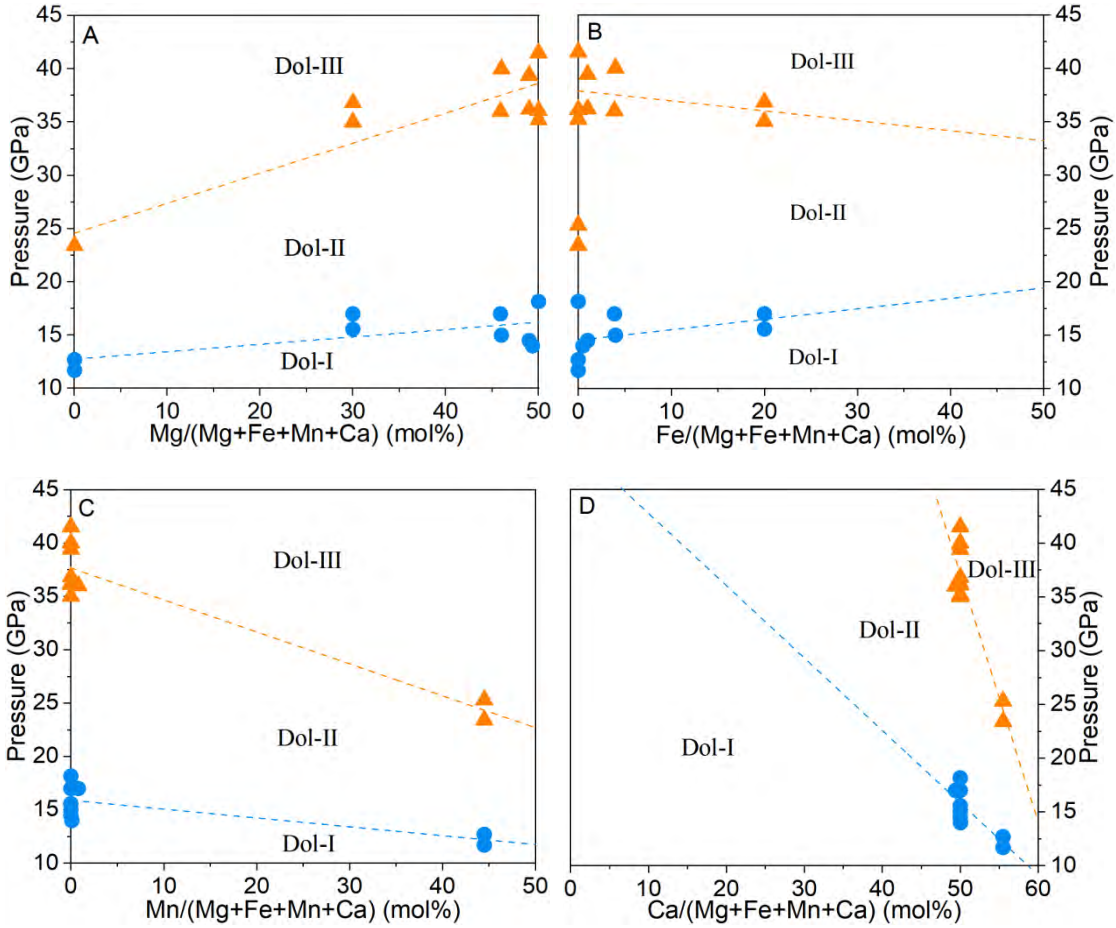

527

528

529 **Figure 7.** Cation radius effects on the phase transitions from Dol-I to Dol-II and then to Dol-III
530 at room temperature. (A) Mg, (B) Fe, (C) Mn, and (D) Ca over the total Mg+Fe+Mn+Ca. All the
531 plotted experimental data are listed in **Table 2** with the use of He or Ne as a PTM to avoid the
532 effect of non-hydrostaticity on the phase transitions in $Ca(Mg,Fe,Mn)(CO_3)_2$. The linear fitting
533 represents the phase transitions from Dol-I to Dol-II (blue) and then to Dol-III (orange).

534

This is the peer-reviewed, final accepted version for American Mineralogist, published by the Mineralogical Society of America.
The published version is subject to change. Cite as Authors (Year) Title. American Mineralogist, in press.
DOI: https://doi.org/10.2138/am-2022-8248. http://www.minsocam.org/

535 **Table 1.** Vibrational properties of $Ca_{1.11}Mn_{0.89}(CO_3)_2$ at high pressure and room temperature with
536 the use of helium as a pressure-transmitting medium.

Raman modes	Dolomite-I (0–12.7 GPa)		II (12.7–23.4 GPa)		III (23.4–50.0 GPa)	
	ν_{0i} (cm^{-1})	$d\nu_i/dP$	ν_{0i} (cm^{-1})	$d\nu_i/dP$	ν_{0i} (cm^{-1})	$d\nu_i/dP$
T	167	3.07(6)	211	4.24(41)	140	0.13(3)
					152	0.74(6)
					184	0.60(24)
L	287	4.81(12)	305	3.62(37)	310	1.82(24)
			353	3.52(41)	348	2.05(17)
			413	4.10(43)	393	2.62(34)
ν_4	718	1.62(9)	738	2.35(33)	761	0.58(12)
ν_2	872	-0.49(7)	867	-0.60(5)	850	-0.10(2)
ν_1	1088	3.37(8)	1132	3.04(4)	1146	1.39(9)
					1164	1.50(14)
					1174	2.17(4)

537 The ν_{0i} modes of $Ca_{1.11}Mn_{0.89}(CO_3)_2$-I, -II, and -III represent the Raman peaks at 0, 13.7, and
538 24.3 GPa, respectively, at room temperature.
539

Table 2. Phase transitions of the dolomite group at high peressure and room temperature in the pressure-transmitting medium (PTM) of He or Ne.

Composition	Dol-Ib (GPa)	Dol-II (GPa)	Dol-III* (GPa)	Method	PTM	References
$CaMg(CO_3)_2$	-	-	36.1(25)	Raman	He	This study
$CaMg(CO_3)_2$	-	-	35.2(10)	Raman	Ne	This study
$Ca_{1.11}Mn_{0.89}(CO_3)$	-	12.7(15)	23.4(13)	Raman	He	This study
$Ca_{1.11}Mn_{0.89}(CO_3)$	-	11.7(16)	25.3(8)	Raman	Ne	This study
$CaMg_{0.98}Fe_{0.02}(CO_3)_2$	9.1	14.5	36.2	Raman	Ne	Binck et al. (2020b)
$CaMg_{0.98}Fe_{0.02}(CO_3)_2$	-	20.5	43.4 (III*c*)	XRD	Ne	Binck et al. (2020b)
$CaMg_{0.98}Fe_{0.02}(CO_3)_2$	-	-	39.4	Raman	Ne	Efthimiopoulos et al. (2018)
$CaMg_{0.92}Fe_{0.08}(CO_3)_2$	-	15	40	Raman	Ne	Vennari and Williams (2018)
$CaMg(CO_3)_2$	-	18.2	41.5 (III*c*)	XRD	Ne	Merlini et al. (2017)
$CaMg_{0.6}Fe_{0.4}(CO_3)_2$	-	15.6	36.8 (III*b*)	XRD	Ne	Merlini et al. (2017)
$CaMg_{0.6}Fe_{0.4}(CO_3)_2$	-	17	35 (III*b*)	XRD	Ne	Merlini et al. (2012)
$Ca_{0.988}Mg_{0.918}Fe_{0.078}Mn_{0.016}(CO_3)_2$	-	17	36	XRD	Ne	Mao et al. (2011)
$Ca_{1.001}Mg_{0.987}Fe_{0.01}Mn_{0.002}(CO_3)_2$	-	14	-	XRD	Ne	Zucchini et al. (2014)

Asterisk (*): For iron-free or -poor dolomite, the Dol-III phase corresponds to the Dol-IIIc (space group $P\bar{1}$ with $Z = 8$); for iron-rich dolomite, the Dol-III phase corresponds to the Dol-III*b* (space group $R\bar{3}$ with $Z = 3$) based on XRD measurement (Binck et al., 2020b).